

Curvature effects in turbulent premixed flames of H₂/Air: a DNS study with reduced chemistry

G. Rocco · F. Battista · F. Picano · G. Troiani · C.M. Casciola

Received: date / Accepted: date

Abstract Data from a three-dimensional Direct Numerical Simulation of a turbulent premixed Bunsen flame at a low global Lewis number are analyzed to address the effects of the curvature on the local flame front. For this purpose, the chemical kinetics is modeled according to a reduced scheme, involving 5 reactions and 7 species, to mimic a H₂/Air flame at equivalence ratio $\phi = 0.5$. An increase of the local temperature and reaction rate is found for fronts elongated into the fresh gases (concave), while local quenching is observed for fronts elongated in the opposite direction (convex), i.e. towards the burnt mixture. Data show that the occurrence in the reaction region of these super-reactive (concave fronts) and quenched zones (convex fronts) is predominant compared to a behavior compatible with the corresponding unstretched laminar flame. In particular, well inside the reaction region, the probability density function of the OH radical concentration shows a bi-modal shape with peaks corresponding to negative (concave) and positive (convex) curvatures, while a locally flat front is less frequently detected. The two states are associated with a higher and lower chemical activity with respect the laminar case. Additional statistics conditioned to the local hydrogen concentration provide further information on this dual-state dynamics and on the differences with respect to

G. Rocco
Department of Aeronautics, Imperial College London, South Kensington Campus, London SE7 2AZ, UK

F. Battista · C.M. Casciola
Department of Mechanical and Aerospace Engineering, La Sapienza University, via Eudossiana 18, 00184, Roma, Italy

F. Picano
Department of Industrial Engineering, University of Padova, Via Venezia 1, 35131 Padua, Italy E-mail: francesco.picano@unipd.it

G. Troiani
Sustainable Combustion Laboratory, ENEA C.R. Casaccia, via Anguillarese 301, 00123 Roma, Italy

the corresponding laminar unstretched flame when moving from the fresh to the burnt gas regions. Finally we discuss the effects of the turbulence on the thermo-diffusive instability showing that the turbulent fluctuations, increasing the flame front corrugations, are essentially responsible of the local flame quenching.

Keywords DNS · turbulent premixed flames · Hydrogen · flame instability

1 Introduction

An increasing concern for the environment and the rising cost of fossil fuels are driving modern designers to consider different types of fuels for power production or transport systems. Hydrogen and hydrogen-based fuel mixtures, which contain methane, carbon monoxide or small traces of fossil gases (the so-called *syngas* [1]) are among the most promising fuels for applications in the near future. The key features of hydrogen-based fuels are their low polluting emissions, their high reaction heat values and their abundance in the natural environment.

One of the most distinctive features of gaseous hydrogen is its low molecular mass in comparison with that of carbon-bases fuels, which is responsible for its faster diffusion speed. The high mass diffusion of hydrogen strongly influences mixing and combustion processes, and induces the thermo-diffusive instabilities, which may cause local flame quenching and high temperature fluctuations [2, 3, 4, 5, 6, 7]. Within the framework of combustion theory, the effects of mass diffusion are properly described by the Lewis number [3, 8, 9, 10, 11, 12], namely the ratio between the heat and the mass diffusion coefficients, which properly summarizes the instability characterizing the flame behavior. When a mixture is composed of several species with different transport coefficients, the global Lewis number is assumed to be equal to the Lewis number of the less abundant species in the mixture, evaluated with respect to the stoichiometric balance [13]. When the Lewis number is much lower than one, thermo-diffusive instabilities occur; there are consequent quenching effects in the local flame and the appearance of regions where the reactions peak. This phenomenon has been properly explained in the context of a laminar flame [14].

Using a simplified chemistry, Chakraborty et al. [3] studied the effects of the global Lewis number on the scalar transport properties for some turbulent premixed flames. Three-dimensional Direct Numerical Simulation (DNS) of the statistically planar flames were performed in a wide range of different Lewis numbers, above and below the critical value $Le = 1$. In these simulations, the flames with $Le \ll 1$ exhibited strong counter-gradient transport effects, while the gradient transport (Fick-like law) was detected when the Lewis number was increased. Here counter-gradient transport is taken to imply $J_D \cdot \nabla c > 0$, as opposed to Fick-like transport where $J_D \cdot \nabla c < 0$, with J_D the diffusive flux and c the concentration. Although Chakraborty et al. have addressed the effects of a properly defined global Lewis number on flames in realistic configurations,

the local effects due to the different mass diffusivity of the chemical species was not considered.

A similar configuration, though two-dimensional, is used in Chakraborty et al. [15] to address the correlation between the strain rate and the curvature, and their effects on the surface density function. Their analysis takes into account two turbulent premixed flames of lean methane-air and hydrogen-air mixtures. Data are obtained by means of Direct Numerical Simulations and a suitably detailed scheme is used to model the chemistry. The authors compare the statistics of methane-air and hydrogen-air flames and investigate the effects of thermochemistry and preferential diffusion on the surface density function. The surface density function, $\sigma = |\nabla c|$ is an important observable in turbulent premixed flames since it is strictly correlated to the dissipation rate, $\chi = D\sigma^2$, which is crucial in turbulent combustion modeling [16].

A similar geometry is investigated in [17], where DNS of hydrogen-air turbulent premixed flames is used to investigate the local flame structure and the fractal characteristics. The authors show the strong dependence of the flame structure on the Reynolds number: local quenching is seen to increase with the Reynolds number.

Im & Chen [18] discuss the interaction of premixed flames with two dimensional turbulence by performing two numerical simulations. They compare a lean and a rich hydrogen/air premixed flame, showing the opposite effect of the curvature and strain on the chemical activity of the two flames. The effects of thermo-diffusive instability on the initially planar two dimensional hydrogen flame is investigated in [19]. The authors perform the 1D and 2D simulations of a lean premixed hydrogen flame, showing that even a 2D initially planar flame is unstable, self inducing flame wrinkling and fluctuations. A wider analysis on the statistically planar turbulent flame in 3D is reported in [2, 20]. The authors address the behavior of a lean premixed hydrogen flame reporting the effects of Karlovitz number, Ka , and equivalence ratio, ϕ , on the flame instability (the cellular flame regime). They observe that at high Karlovitz number the distributed flame regime occurs showing a broad flame front which is similar to a mixing region.

Wang et al. [6] have investigated the effects of a swirling flame on the preferential diffusion in hydrogen-air flames, showing that the swirl tends to suppress the effects of the preferential diffusion.

The purpose of the present study is to investigate the effects of the preferential diffusion of hydrogen on a Bunsen turbulent premixed air flame focusing on the effect of turbulent fluctuations on the local flame dynamics. The hydrogen/air mixture is provided by a fully developed turbulent pipe flow obtained by a companion simulation which carries *real* turbulent fluctuations at the Bunsen inlet. The present geometry, being well replicable in experiments, represents a step forward in direct numerical simulations of turbulent combustion.

Consistently with previous studies [18, 2, 20], we found the typical cusp-like structures of the flame front protruding towards products associated with quenched regions, while opposite structures induce super-burning regions. We statistically characterize this behavior in the turbulent regime highlighting the

differences among the local turbulent flame structure, the unstrained laminar flame and the laminar (cellular) flame subjected only to thermo-diffusive instability. To this end, we provide joint-pdf among local flame front curvature, local velocity gradient, concentration of OH radicals, and hydrogen atomic equivalence ratio with respect to laminar cases.

All the statistics are conditioned to different intervals of the local hydrogen concentration allowing a study of the process from the beginning to the end of the reaction region and a direct comparison with the unstretched laminar flame. Well inside the local flame, we show that the dynamics strongly differs from the corresponding unstrained premixed flame and two different burning states are typical. One is a super-burning cell with high chemical activity and temperature higher than adiabatic; the other corresponds to an almost quenched region. The local state is mainly determined by the local curvature of the flame front. A comparison between the turbulent and the corresponding laminar Bunsen flame is provided to assess the effects of turbulence on the front dynamics. Although the cellular structure induced by the thermo-diffusive instability of the laminar flame presents super-burning regions resembling those observed in the turbulent flame, quenched regions are considerably less frequent.

The paper is organized as follows. Section § 2 describes the numerical tool employed for the Direct Numerical Simulation of the 3D turbulent flame, the chemical mechanism and the used physical parameters; section § 3 discusses the results obtained from DNS: instantaneous analysis and statistical analyses based on the joint probability density function are used; final remarks and comments are illustrated in the last section § 4.

2 Numerical methodology

2.1 Flow solver

The problem is described by the Navier-Stokes equations in cylindrical coordinates in an open environment at constant pressure p_0 . The governing equations are expanded by means of a low-Mach number asymptotic approximation [21, 22], which, in dimensionless form, read:

$$\frac{\partial \rho}{\partial t} + \nabla \cdot (\rho \mathbf{u}) = 0 \quad (1)$$

$$\frac{\partial \rho \mathbf{u}}{\partial t} + \nabla \cdot (\rho \mathbf{u} \otimes \mathbf{u}) = \frac{1}{\text{Re}} \nabla \cdot \Sigma - \nabla P + \rho \mathbf{g}^* \quad (2)$$

$$\frac{\partial \rho Y_a}{\partial t} + \nabla \cdot (\rho \mathbf{u} Y_a) = \frac{1}{\text{ReSc}_a} \nabla \cdot (\sigma_D \nabla Y_a) + \omega_a \quad (3)$$

$$\nabla \cdot \mathbf{u} = \frac{1}{p_0} \left[\frac{1}{\text{RePr}} \nabla \cdot (\sigma_T \nabla T) + \frac{\gamma - 1}{\gamma} \omega_Q \right] \quad (4)$$

$$T = \frac{p_0}{\rho} \quad (5)$$

where $\Sigma = 2\sigma_\mu(T)\mathbf{E} + \sigma_\lambda \text{tr}(\mathbf{E})\mathbf{I} = \sigma_\mu(T)(\nabla\mathbf{u} + \nabla\mathbf{u}^T) + \sigma_\lambda \nabla \cdot \mathbf{u}\mathbf{I}$ is the viscous stress tensor with σ_λ set to zero and $\sigma_\mu(T) = \mu/\mu_0$ denoting the dimensionless, temperature (T) dependent viscosity. ρ , \mathbf{u} , p_0 and P are the density, the velocity, the thermodynamic pressure, and the dynamic pressure, respectively. We stress that the thermodynamic pressure p_0 is constant in space, due to the low-Mach number expansion [21], and in time, due to the open space conditions. The assumed dimensionless is $p_0 = 1$, corresponding to a pressure of 1 atm. Y_a and ω_a are the concentration and the global reaction rate of the a^{th} species in the mixture. $\sigma_D(T) = D_a/D_a^0$ and $\sigma_T(T) = \alpha/\alpha_0$ are the dimensionless mass and thermal diffusivities. The dynamic viscosity of the mixture at reference conditions (inlet conditions $p = 1\text{atm}$ and $T = 300\text{K}$) is indicated by μ_0 , the Reynolds number is $\text{Re} = \rho_0 U_0 L_0 / \mu_0$, where U_0 and L_0 are the typical velocity and length scales (bulk velocity and radius of the jet in the present case). $\text{Pr} = \mu_0 / (\rho_0 \alpha_0)$ is the Prandtl number at reference conditions. The ratio of the constant pressure coefficient, c_p , and the constant volume coefficient, c_v , is denoted by γ ; the Schmidt number Sc_a for the a^{th} species is defined as the ratio of the viscosity and the binary mass transport coefficient of the specific species a in the most abundant element in the mixture (here taken to be N₂): $\text{Sc}_a = \mu_0 / (\rho_0 \mathcal{D}_{aN_2})$. In these conditions, the Schmidt number only depends on the a -th specie and on the most abundant one (at reference conditions), see [14] sec. 5.2.4.1. Details on the values of the parameters and the assumptions used in modeling the mass diffusion coefficients are given in section 2.2.

The Direct Numerical Simulation (DNS) of the Bunsen flame is performed using second order central finite differences in a conservative formulation on a staggered grid. Bounded Central Difference Schemes [23] are used for the non-linear terms in the scalar equations (1) and (3). Temporal evolution is performed by a low-storage third order Runge-Kutta scheme.

Time-dependent boundary conditions are prescribed for the inflow. For this purpose, a fully turbulent inflow velocity is dynamically assigned by means of a cross-sectional slice of a fully developed pipe flow simulation. Indeed, the inflow condition is obtained by a companion simulation of a fully turbulent periodic pipe flow from which the turbulent velocity profile in a cross-sectional slice is extracted at each time step and enforced at the inlet surface of the jet. This allows a realistic turbulent inlet. The computational domain consists of a cylinder: the flow is injected in one base and streams out at the other end. Injection occurs through an orifice in the impermeable and adiabatic base of the domain, see figure 1 panel (a). The density and concentrations of the species are constant and uniform along the inflow orifice. A convective Orlanski [24, 25] condition is adopted at the outflow section. The lateral surface of the cylinder is modeled by an adiabatic traction-free [26] condition, which makes the entrainment of external fluid possible.

The numerical integration starts knowing the density ρ^n , momentum $(\rho\mathbf{u})^n$, and species mass fraction $(\rho Y_a)^n$ fields at a generic time step n . We remark once more that, for low-Mach number expansion and the present open environment configuration, the thermodynamic pressure is constant both in

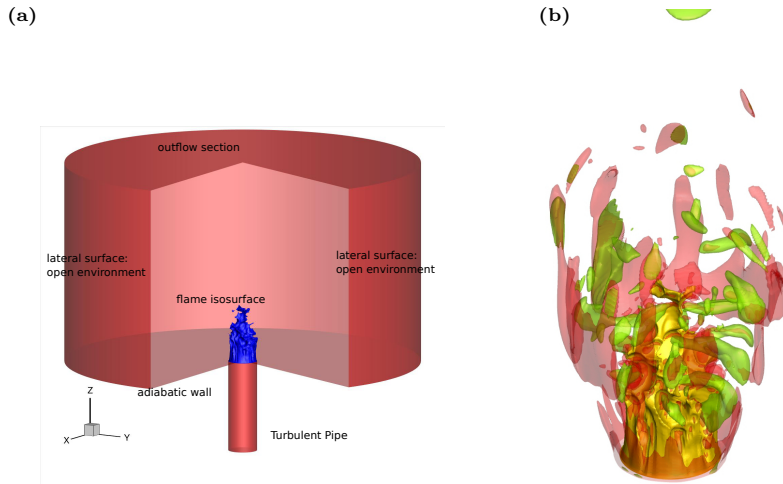


Fig. 1 Panel (a) reports a sketch of the domain geometry with the isosurface (in blue) of the hydrogen mass fraction. Panel (b) reports an instantaneous flame configuration. Yellow: hydrogen mass fraction isosurface, $Y_{\text{H}_2} = 0.01$; green: NO mass fraction isosurface, $Y_{\text{NO}} = 5.9 \times 10^{-8}$; red: water mass fraction isosurface $Y_{\text{H}_2\text{O}} = 0.3$

space and in time. Hence given the density ρ^n , the temperature T^n can be evaluated through the equation of state, eq. (5). The main lines of the solution algorithm are listed below,

- The mass conservation equation is used to integrate the fluid density at time step $n + 1$, ρ^{n+1} .
- The momentum equation (deprived of the hydrodynamic pressure term) is used to find the unprojected velocity field, $(\rho\mathbf{v})^{n+1}$.
- The species continuity equation is used to advance in time $(\rho Y_a)^{n+1}$. We remark that the source terms in species equations are only function of temperature, pressure, and species mass fractions at the time step n .
- The velocity is then projected enforcing the local value of the divergence which depends on the diffusive temperature flux and combustion heat release. The projection method is the straightforward extension of the classical Chorin's method usually employed for fully incompressible Navier-Stokes equations integration. This step requires the solution of a linear system which is solved using the SuperLU Library [27].

The numerical code has been fully tested in several configurations ranging from cold incompressible jets, see e.g. [25, 28, 29], to reactive premixed Bunsen flames, see e.g. [30, 31, 22].

2.2 Reduced chemical model

The chemical kinetics model is known to deeply affect the dynamics of the flame. Although global chemistry schemes facilitate the incorporation of com-

plex chemical features into turbulent simulations, the absence of intermediate radicals is unsuitable for addressing instabilities and extinction phenomena. In this work, a reduction of the original mechanism included in GRI-mech 2.1 [32] is employed. The reduced mechanism implemented is made by 5-step and includes 4 radicals (H, O, OH, NO) besides the main reactants (H₂, O₂, H₂O, N₂) [33] and reads:

1. $\text{H} + \text{O} \rightleftharpoons \text{OH}$
2. $\text{H} + \text{O}_2 \rightleftharpoons \text{OH} + \text{O}$
3. $\text{H}_2 + \text{OH} \rightleftharpoons \text{H}_2\text{O} + \text{H}$
4. $\text{H}_2 + \text{O} \rightleftharpoons \text{H} + \text{OH}$
5. $\text{N}_2 + \text{O}_2 \rightleftharpoons 2\text{NO}$.

The GRI-mech scheme includes results published in the most recent literature and has been validated in a wide range of physical conditions (temperature between 1000 and 2500 K, pressure from 10 Torr to 10 atm) and equivalence ratios (ϕ from 0.1 to 5 for premixed systems). One of its advantages is its optimized chemical kinetics, which includes, via a quasi-steady state and local equilibrium assumptions, the effects of a larger number of elementary reactions on the target species. However, the quasi-steady state assumption concerning the kinetics of the H₂, O₂ and HO₂ might lead to some inaccuracies in the ignition of the mixture at moderate temperatures and high pressures [14]. This effect is not deemed crucial for the present work since the assumed pressure and temperatures are $p = 1 \text{ atm}$, $300 \text{ K} < T < 1550 \text{ K}$ respectively and the emphasis is on the statistically steady state rather than ignition. The complete GRI-mech scheme includes helium, neglected in the present simulations since its role is mainly confined to the generation of pollutants, a subject beyond the scope of this paper. The formation enthalpies of the species Δh_f^0 have been chosen from the NASA-Lewis and the Technion archives. Their values are used to compute the heat release $\omega_Q = -\sum_{a=1}^{N_s} \Delta h_{f,a}^0 \dot{\omega}_a$, where N_s is the number of species and $\dot{\omega}_a$ their respective global production rate.

Binary mass diffusion coefficients \mathcal{D}_{jk} of species j into species k may have an impact on the flame structure, as well as on the formation and evolution of thermo-diffusive instabilities. The exact evaluation of these coefficients has an enormous computational cost since it requires the resolution of an $N_s \times N_s$ linear system at each grid point and time instant. This results in a strong limitation for approaches like DNS, where a huge number of grid points and small time steps are needed to describe the finest scales of the turbulent flame. A viable alternative is Fick's diffusion, whose adoption is here motivated in terms of the *Hirschfelder and Curtiss approximation* [34]. The equivalent diffusion coefficient D_a of a single species into the rest of the mixture [13] is given by

$$D_a = \frac{1 - Y_a}{\sum_{j \neq a} X_j / \mathcal{D}_{aj}} \quad (6)$$

where X_j is the mole fraction of the generic species j and can be reduced with reasonable accuracy to the binary diffusivity of species j into nitrogen,

$D_a \simeq \mathcal{D}_{aN_2}$, due to the excess of N_2 in the air mixture, see [14] section 5.2.4.1 or [13] section 1.1.5. The binary diffusion coefficients \mathcal{D}_{aN_2} can be evaluated using the assumption of binary collisions, which holds when the gas is sufficiently diluted, hence ternary and higher order collisions are rare enough that their effects can be neglected [14]. Clearly, as a counterpart to the substantial reduction in computational complexity, small errors in the diffusion should be tolerated near the flame front. Despite the strong simplification, the diffusivity still strongly depends on the temperature. In the present case, the temperature dependence is accounted for fixing the Schmidt number, $Sc_a = \mu_0/(\rho_0 \mathcal{D}_{aN_2})$, such that the mass diffusivities and the thermal diffusivity inherit the temperature dependence of the dynamic viscosity $\sigma_\mu(T) = \sigma_a(T) = \sigma_T(T) = (T/T_0)^{0.5}$, which follows from a Sutherland-like law. The proportionality is fixed by evaluating the diffusion coefficients at 298 K (see table 1).

Species	$\mathcal{D}_{k,N_2} [m^2/s]$	Sc_k
H ₂	$8.56 \cdot 10^{-5}$	0.175
O ₂	$5.931 \cdot 10^{-6}$	2.53
H ₂ O	$1.218 \cdot 10^{-5}$	1.232
H	$2.136 \cdot 10^{-4}$	0.13
O	$1.094 \cdot 10^{-4}$	0.134
OH	$3.308 \cdot 10^{-5}$	0.45
NO	$5.625 \cdot 10^{-6}$	2.66
He	$3.06 \cdot 10^{-6}$	0.49

Table 1 \mathcal{D}_{k,N_2} and $Sc_a = \mu/(\rho \mathcal{D}_{a,N_2})$ are the binary diffusion coefficients and the Schmidt numbers evaluated for the a specie with respect to molecular nitrogen N_2 at 298K, respectively.

Due to the excess of N_2 , the dependence of γ on the composition of the mixture may also be safely neglected and, given the involved temperature range (burnt/unburnt gas temperature ratio $T_b/T_u \simeq 5$), the constant value $\gamma = 1.25$ can be considered a reasonable approximation [13].

Representative computational results for a one-dimensional, planar, and stationary flame at $\phi = 0.5$ are reported in figure 2. The parameters of this preliminary simulation match the fully 3D ones that will be presented in the following section. The adiabatic flame temperature $T_{ad} \simeq 1555 K$ and the flame speed $S_L = 0.35 m/s$ are consistent with the available results in the literature, see e.g. [14]. The top panel of figure 2 represents the mass fractions as a function of the streamwise coordinate. At this equivalence ratio, hydrogen is completely consumed, while about 48% of O_2 does not react. The narrow reaction zone spans the region extending from $x = 0.002 m$ to $x = 0.0035 m$ where the radical concentrations are more prominent. The concentration of the radical OH can be used to detect the reaction, as in experimental measures on H₂-lean flames [33]. The ability of the radical OH to mark the progress of the reaction is confirmed by the bottom panel of figure 2 which shows the OH-mass fraction, Y_{OH} , as a function of the H₂ mass fraction, Y_{H_2} . This

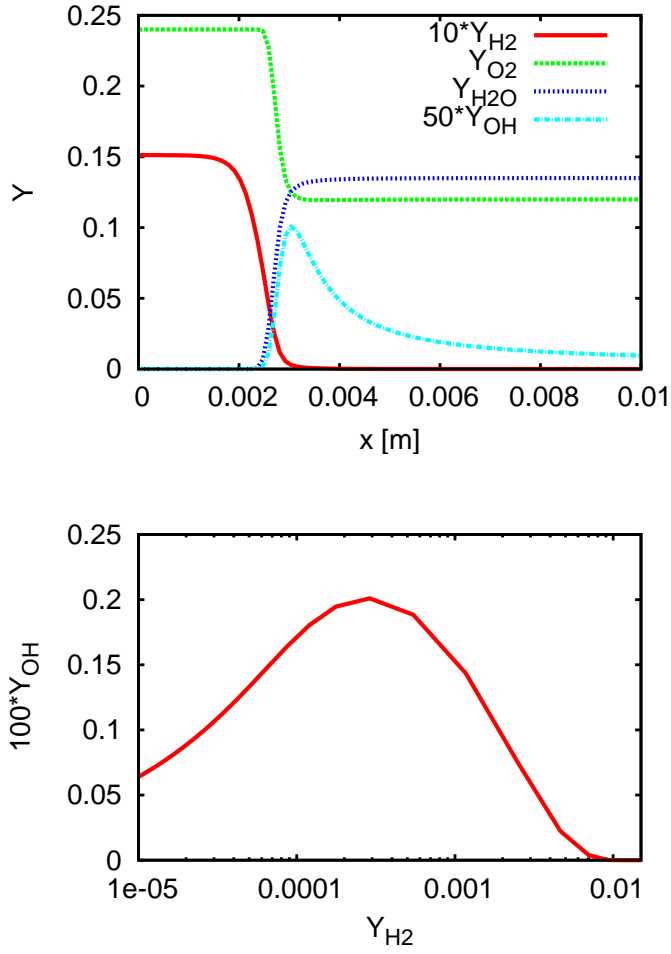


Fig. 2 One-dimensional flame at $\Phi = 0.5$. Top panel, mass fractions Y_k of reactants, products and OH radical vs dimensional distance. Bottom panel, OH mass fraction Y_{OH} with respect to the mass fraction of molecular hydrogen Y_{H_2} .

relation is valid for the one-dimensional laminar planar flames and will be referred as $Y_{OH} = Y_{OH}^L(Y_{H_2})$. When the reaction progresses, H_2 is consequently consumed and the OH mass fraction abruptly increases and reaches a peak at $Y_{H_2} = 2 \times 10^{-4}$ when all the fuel is almost burnt. Afterwards the OH mass fraction starts a more gradual decrease as a consequence of slow recombination phenomena.

The reason for our detailed description of the one-dimensional laminar flame is related to the forthcoming use of the local turbulent fluctuations of OH mass fraction $Y_{OH}(\mathbf{x}, t)$, evaluated with respect to the laminar case, to measure the local activity of the combustion in the turbulent flame. The

procedure is based on a statistical sampling of OH and H₂ concentrations in the turbulent flame. Given a generic turbulent event where the concentration of OH and H₂ are $Y_{\text{OH}}^T, Y_{\text{H}_2}^T$ respectively, we associate the corresponding laminar state $Y_{\text{OH}}^L(Y_{\text{H}_2}^T)$, where the function $Y_{\text{OH}} = Y_{\text{OH}}^L(Y_{\text{H}_2})$ is the profile of the OH concentration in the laminar flame (see bottom panel of figure 2).

A positive/negative deviation with respect to the flamelet mass fraction (flamelet fluctuation),

$$Y'_{\text{OH}} = Y_{\text{OH}} - Y_{\text{OH}}^L|_{Y_{\text{H}_2}}, \quad (7)$$

denotes more/less chemical activity with respect to the corresponding laminar state. It is worth to remark that this observable allows to highlight the differences between the local turbulent flame and the corresponding laminar unstretched flame. More specifically, the comparison is exerted by providing the deviation of the local turbulent quantities from the laminar ones at the corresponding state defined by the same hydrogen concentration Y_{H_2} .

2.3 Direct Numerical Simulation details

The parameters used in the DNS have been chosen to reproduce a laboratory scale premixed Bunsen flame of a lean H₂-Air mixture. The fuel is issued from a pipe whose radius is $R = 0.009$ m; the bulk velocity is $U_0 = 5$ m/s and the equivalence ratio is $\phi = 0.5$. The surrounding environment is filled by pure air at the same temperature of fresh gas, i.e. $T = 298$ K. The Reynolds number is $\text{Re}_R = U_0 R / \nu_\infty = 3000$ while the Prandtl number is $\text{Pr} = \nu_0 / \alpha_0 = 0.6$, where ν_0 and α_0 are the inflow kinematic viscosity and the thermal diffusivity of the mixture, respectively. The Froude number, taking into account the buoyancy effects, is fixed at $Fr = U_0 / \sqrt{gR} = 16.8$. The Damköhler and Karlovitz numbers at the inflow are $Da = L_t S_L / (u' \delta_L) \simeq 22.3$ and $Ka = \delta_L u_\eta / (\eta S_L) \simeq 0.65$, respectively. Here L_t and u' are the integral length and the velocity root-mean-square (bulk) fluctuations, while η and u_η are the Kolmogorov length and velocity, respectively. The computational domain $[\theta_{max} \times R_{max} \times Z_{max}] = [2\pi \times 12R \times 14R]$ is discretized using a mesh of $N_\theta \times N_r \times N_z = 128 \times 201 \times 560$ collocation points, endowed with a suitable radial stretching to properly capture the shear layers and the flame front dynamics. The characteristic grid spacing near the nozzle exit is $\Delta \simeq 2\eta_k$, where η_k is the Kolmogorov length scale near the wall of the adjoining pipe; the grid spacing was chosen such that at least four grid points are located across the instantaneous flame front. Additional details and comparisons with experimental data can be found in [30, 31], where an identical numerical setup is used to simulate a Bunsen premixed flame using a global reaction model.

Two 3D simulations have been performed and analyzed. The former reproduces a turbulent Bunsen flame by enforcing a turbulent inflow velocity endowed with turbulent fluctuation extracted from a companion turbulent pipe simulation; the second one reproduces the laminar (cellular) Bunsen flame by prescribing a parabolic velocity profile at the jet inlet. All other parameters are the same for the two simulations to directly assess the effects induced by the

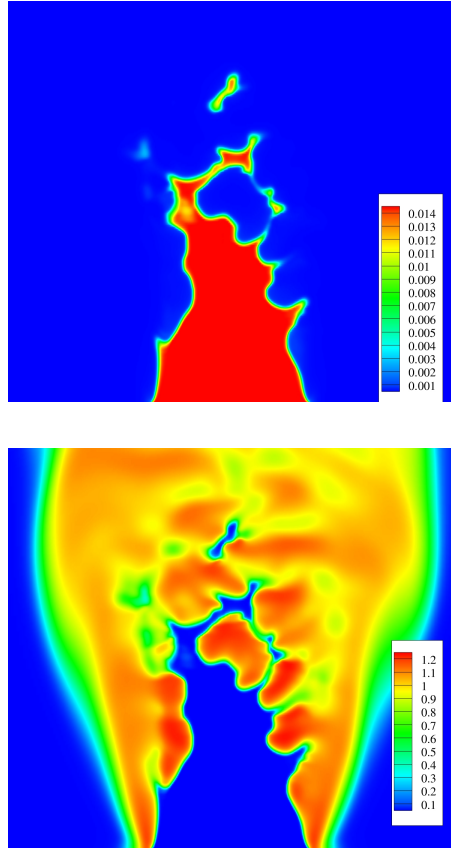


Fig. 3 2D snapshots of the concentration of molecular hydrogen Y_{H_2} , top panel, and of the progress variable based on the temperature $c_T = T - T_u / (T_{ad} - T_u)$ (T temperature, T_{ad} adiabatic flame temperature, T_u unburned mixture temperature), bottom panel.

turbulent fluctuations. The turbulent flame simulation spans about $4.5 R/U_0$ time scales in the statistical steady state to collect about 60 uncorrelated fields every $0.075 R/U_0$ to calculate the statistics.

3 Results

3.1 Instantaneous configurations

This section describes the instantaneous behavior of the turbulent flame, focusing on the interaction between turbulence and chemistry and the effects of preferential diffusion.

The top panel of Fig. 3 shows the contours of the molecular hydrogen concentration Y_{H_2} , on a plane containing the jet axis extracted from the instantaneous three-dimensional field. The thin green layer corresponds to the flame

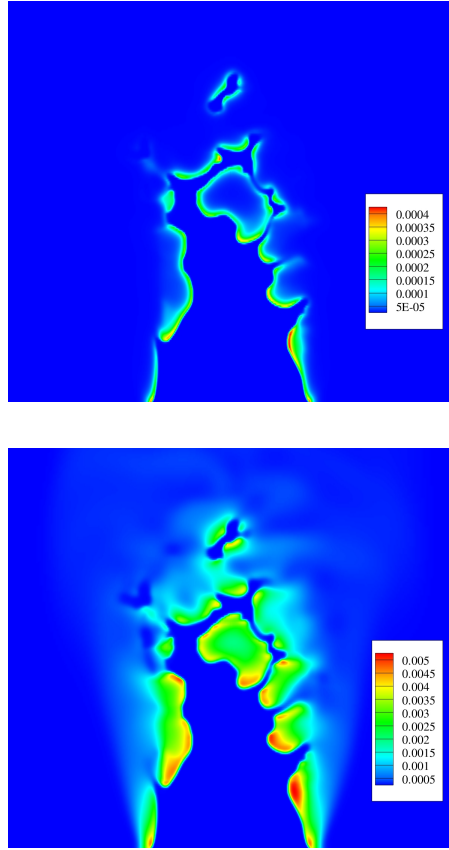


Fig. 4 2D snapshots of the concentrations of the radicals Y_H and Y_{OH} , top and bottom panels, respectively.

front; Y_{H_2} shows large variations along the front, moving from the fresh mixture to the products. The front is severely wrinkled by the turbulence, to the extent that pockets of fresh gas are turned off and carried into the product side where they may be eventually consumed. The flame front can be parametrized in terms of a temperature-based progress variable $c_T = (T - T_u)/(T_{ad} - T_u)$, where T_{ad} is the adiabatic flame temperature of the inlet mixture and T_u is the temperature of the unburnt mixture.

Two different types of structures identify the flame front: the *gullies*, i.e. the narrow regions concave towards the fresh gas, and the *bulges*, i.e. the larger, smoother regions convex towards the fresh gas [35,36]. The bulges are characterized by values of c_T significantly exceeding unity, up to 1.2 (super-adiabaticity), whereas sub-adiabatic conditions, $c_T < 1$, occur in gullies, even in regions where the hydrogen concentration Y_{H_2} is very low. In both regions, the isolevels of Y_H , Y_{OH} follow the flame front closely, as shown in figure 4, confirming their role as good markers of the progress of combustion, see e.g.

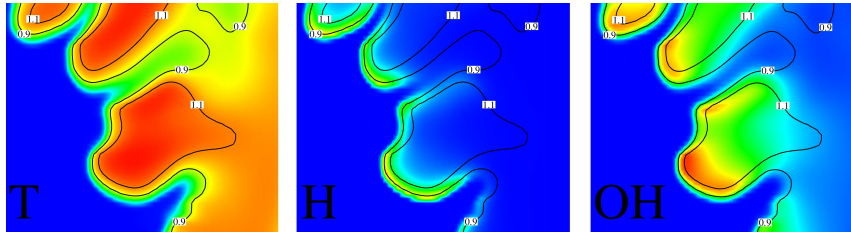


Fig. 5 2D snapshot enlargements of T (left), Y_{H} (middle) and Y_{OH} (right). Isolines are two isolevels of c_T : 0.9 and 1.1, respectively. The color maps match those of figure 3 and 4.

[35,37,38]. The Y_{H} concentration profile appears to be symmetric with respect to the peak concentration values and tends to be localized near the flame front. Y_{OH} displays a completely different behavior since it sharply grows at the beginning of the flame front and slowly decreases towards the hot gas region, so that OH radical persists well inside the burnt region. The high concentration of radicals in the bulges attests to the intense chemical activity in these regions, while their absence in the gullies is an indication of flame quenching. Figure 5 shows two isolines of the progress variable c_T overlapping with the contour plot of the concentrations of the radicals. The almost exact parallelism of the isolines resembles the lamellar structure observed in the experimental results of Chen and Bilger [35,36]. The isolines appear to be closer in the bulges than in the gullies, indicating steeper temperature gradients $|\nabla c_T|$, which are related to a reduction of the flame thickness $\delta \sim 1/|\nabla c_T|$ and an intensified scalar dissipation rate $\chi \sim |\nabla c_T|^2$ [39]. Smoother temperature gradients in the gullies are associated with reduced concentrations of the radicals and the presence of significant quenching effects. Turbulent fluctuations enhance flame corrugation which, however, is also known to occur in two dimensional simulations and experiments [40,41] on laminar flames. Indeed lean hydrogen flames are strongly subject to differential diffusion and thermo-diffusive instabilities [42], which are responsible of the flame wrinkling, temperature oscillations and possible local extinctions, independently of the turbulent or laminar regime. This type of instability is associated with the high diffusivity of the molecular hydrogen H₂ and a consequent very low Lewis number, $Le = D_T/D_{\text{H}_2} \ll 1$. Hydrogen diffuses towards the burnt gases much faster than heat diffuses towards the fresh gases. The ratio of hydrogen to temperature diffusion lengths is the inverse square root of the Lewis number, $\delta_{\text{H}_2}/\delta_T = 1/\sqrt{Le}$. This effect, combined with the local curvature of the front, implies the local enrichment of the mixture in the tiny diffusively heated region (i.e. the bulges). Consequently, the burnt temperature of the gas exceeds the corresponding temperature of the laminar planar flame. In gullies, due to the opposite curvature, reactants diffuse in a large zone, resulting in a decrease in the temperature of the flame. The presence of both positive and negative curvatures induces an unstable situation [13], which is further enhanced by the turbulent fluctuations.

3.2 Statistical analysis

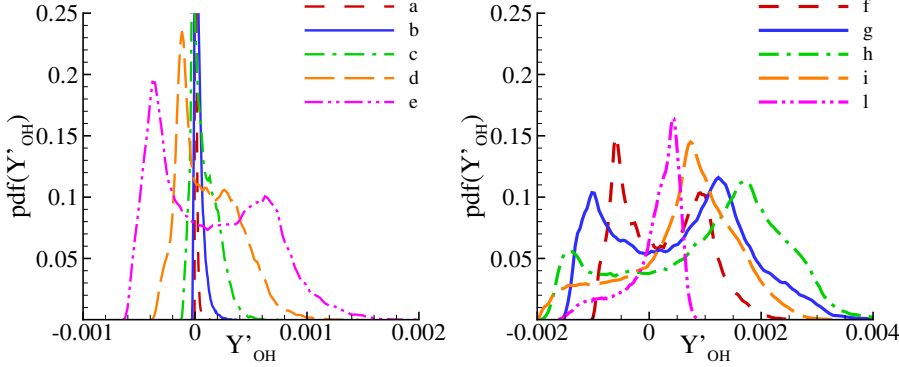


Fig. 6 Probability density function of the OH radical mass fraction flamelet fluctuation, see eq. (7), at different H_2 concentration intervals: (a) $1 \times 10^{-2} \leq Y_{H_2} \leq 1.2 \times 10^{-2}$. (b) $8 \times 10^{-3} \leq Y_{H_2} \leq 1 \times 10^{-2}$; (c) $6 \times 10^{-3} \leq Y_{H_2} \leq 8 \times 10^{-3}$; (d) $4 \times 10^{-3} \leq Y_{H_2} \leq 6 \times 10^{-3}$; (e) $3 \times 10^{-3} \leq Y_{H_2} \leq 4 \times 10^{-3}$; (f) $2 \times 10^{-3} \leq Y_{H_2} \leq 3 \times 10^{-3}$; (g) $1 \times 10^{-3} \leq Y_{H_2} \leq 2 \times 10^{-3}$; (h) $5 \times 10^{-4} \leq Y_{H_2} \leq 1 \times 10^{-3}$; (i) $1 \times 10^{-4} \leq Y_{H_2} \leq 5 \times 10^{-4}$; (l) $5 \times 10^{-5} \leq Y_{H_2} \leq 1 \times 10^{-4}$.

The instantaneous fields showed that combustion in lean hydrogen flames is mainly characterized by two different states: more reactive regions, exhibiting super-adiabatic temperatures (bulges), alternated with nearly quenched areas (gullies), which display lower temperatures. A global characterization, which shows the statistical weight of these two states, can be given in terms of the probability density function (pdf) of the flamelet fluctuation of OH concentration, Y'_{OH} , eq. (7), as shown in figure 6.

As explained in section § 2, Y'_{OH} is defined as the difference of local turbulent concentration of radical OH with that corresponding the same Y_{H_2} in the unstretched laminar flame.

Figure 6 shows the probability density function (pdf) of Y'_{OH} conditioned to different intervals of H_2 concentration. This procedure allows to analyze different regions of the instantaneous reaction zone moving from the fresh gas (high Y_{H_2}) to the burnt region (low Y_{H_2}). Close to the fresh gas region, plots (a), (b), (c), and (d) in the left panel of figure 6, the pdf is characterized by a mono-modal behavior with a slightly negative most frequent state and an intense positive tail. In this part of the flame front the combustion process is reasonably described by a flamelet approximation with the local flame structure similar to the unstretched laminar flame, note the pdf close to a Dirac function centered at the origin. Despite the similarity, the steep positive tails denote intense intermittent events with strong chemical activity that cannot be described in the standard flamelet framework. Proceeding across the flame, plots (e) of left panel and (f), (g), and (h) of right panel, the pdf of Y'_{OH} shows a bi-modal distribution with one maximum in correspondence with negative

and the other with positive fluctuations, respectively. This distribution is inconsistent with the pure flamelet regime whose pdf should appear as a narrow mono-modal distribution centered at the origin. Indeed the flamelet regime corresponds to turbulent flames wrinkled by turbulent fluctuations that locally share the structure of a laminar flame. The present results provide evidence that the flame structure is typically inconsistent with a flamelet. Focusing on plot (g) of fig. 6 for definiteness, the two modal values of the distribution correspond to slow ($Y'_{\text{OH}} \simeq -0.001$) and fast ($Y'_{\text{OH}} \simeq 0.0012$) burning states. They occur almost 50% and 90% more frequently than the unstrained laminar state ($Y'_{\text{OH}} = 0$). The state $Y'_{\text{OH}} \simeq -0.001$ appears to be associated with almost quenched areas since the local radical concentration $Y_{\text{OH}} \simeq Y'_{\text{OH}} + \bar{Y}_{\text{OH}}^L$ almost vanishes ($\bar{Y}_{\text{OH}}^L \sim 0.001$ when $1 \times 10^{-3} \leq Y_{\text{H}_2} \leq 2 \times 10^{-3}$). In the fast burning state, the concentration of OH turns out to be more than twice the laminar value. On the contrary, in the last stage of the turbulent reaction zone (towards the burnt gases), plots (i) and (l) in the right panel of Fig. 6, a mono-modal behavior is recovered, though characterized by a positive mode and an intense negative tail. Indeed, this reaction region is seemingly characterized by higher chemical activity than the laminar flamelet and by strong intermittent events.

The evidence is that the current turbulent lean hydrogen flame can be sketched as a bi-stable system with two distinct states reacting more slowly (nearly quenched) and more quickly than the laminar unstretched flamelet. These events are prevailing in the inner part of the flame and influence the fore and hind reaction region by intermittent intense-burning and quenching events, respectively (pdf tails).

In order to discuss the strong impact that turbulent fluctuations have on the dynamics of the flame, we address the correlations among flamelet fluctuations of the radical OH , velocity gradient and flame curvature. Given the strong gas expansion in the flame, the effect of local deformation induced by turbulence could be blurred by the flow divergence. In these conditions, the statistical characterization of the turbulence-combustion interaction interaction is better achieved by considering the deviatoric part of the strain rate $\mathbf{E}_{\text{dev}} = (\nabla \mathbf{u} + \nabla \mathbf{u}^T) / 2 - (\nabla \cdot \mathbf{u}) \mathbf{I} / 3$, as it appears in the equation for the local stretching rate \varkappa [13],

$$\varkappa = \frac{1}{A} \frac{dA}{dt} = \underbrace{\frac{2}{3} \nabla \cdot \mathbf{u}}_I - \underbrace{\mathbf{n} \otimes \mathbf{n} : \mathbf{E}_{\text{dev}}}_{II} + \underbrace{S_d (\nabla \cdot \mathbf{n})}_{III}. \quad (8)$$

The stretching rate incorporates three different kinematic effects. Besides the gas expansion, which is directly associated with heat released during the combustion (term *I*), two additional terms on the right hand side of equation (8) contribute to the stretching rate: the strain effect, (term *II*), and the mean curvature of the reaction front (*III*). In accordance with equation (8), we have found that these last two terms mostly influence the flame dynamics and they both clearly demonstrate correlation with the chemical activity.

Figure 7 shows the joint-pdf of deviatoric strain rate magnitude, $\mathcal{S}_{dev} = \sqrt{2\mathbf{E}_{\text{dev}} : \mathbf{E}_{\text{dev}}}$, and flamelet fluctuation of the OH radical concentration,

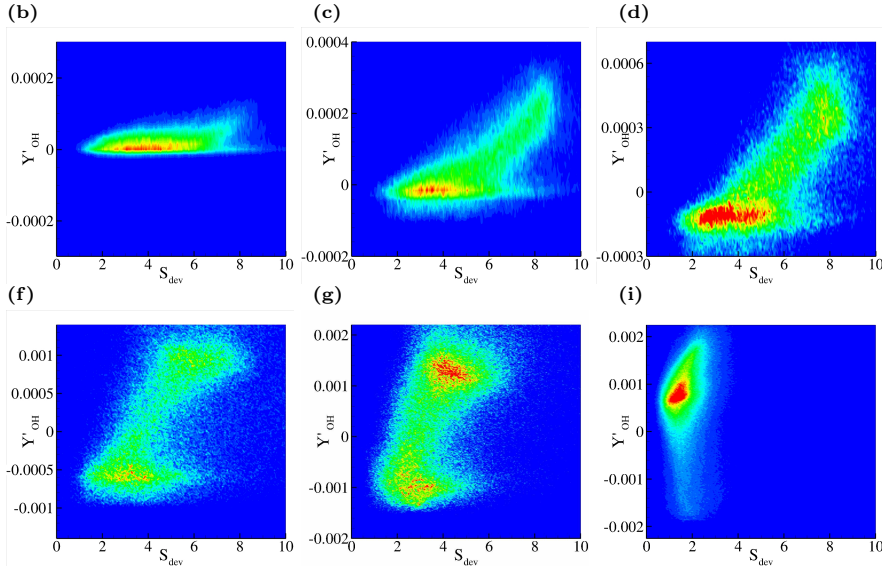


Fig. 7 Joint probability density function (jpdf) of the flamelet normalized OH concentration Y'_{OH} and the deviatoric strain rate $S_{dev} = \sqrt{E_{dev} : E_{dev}}$, normalized by R/U_0 . In order to avoid spurious sampling effects, jpdf are evaluated along the flame front conditioning at different H_2 concentration intervals: (b) $8 \times 10^{-3} \leq Y_{H_2} \leq 1 \times 10^{-2}$; (c) $6 \times 10^{-3} \leq Y_{H_2} \leq 8 \times 10^{-3}$; (d) $4 \times 10^{-3} \leq Y_{H_2} \leq 6 \times 10^{-3}$; (f) $2 \times 10^{-3} \leq Y_{H_2} \leq 3 \times 10^{-3}$; (g) $1 \times 10^{-3} \leq Y_{H_2} \leq 2 \times 10^{-3}$; (i) $1 \times 10^{-4} \leq Y_{H_2} \leq 5 \times 10^{-4}$.

Y'_{OH} . Statistics are presented for six of the ten conditional H_2 concentrations used in figure 6, in particular, the intervals of Y_{H_2} denoted by the letters (b), (c), (d), (f), (g), and (i). The aft part of the flame (towards the fresh mixture, high H_2 concentration) is substantially unaffected by the deviatoric strain, with OH radical concentration following the behavior of the unstretched, laminar flamelet. Moving inside the reaction region ((c) and (d) panels) an high deviatoric strain promotes intense chemical activity, i.e. Y'_{OH} is positive. In the hind part of the flame (panels (f) and (g)), the positive $Y'_{OH} - S_{dev}$ correlation indicates that strong burning states are associated with high deviatoric strain rates. This correlation reduces moving further towards the burnt region to become very weak in panel (i) where the mixture is almost entirely burnt. The positive mode of Y'_{OH} clearly shows the higher OH radical concentration found in the outer part of the turbulent flame (product side) in comparison with the reference flamelet.

In order to distinguish the contribution of the different components of the strain rate, the top panel of figure 8 addresses the joint pdf (jpdf) of Y'_{OH} and the deviatoric strain rate component aligned to the flame normal \mathbf{n} , $D_{nn} = \mathbf{E}_{dev} : \mathbf{n} \otimes \mathbf{n}$, term II of equation (8). Near the fresh gas, panels (b) and (c), a weak positive correlation is detected. Moving through the front towards the burnt gas, we observe an increasing positive correlation, see e.g. panel (d). In the middle of the flame front, panels (f) and (g), the now familiar bi-

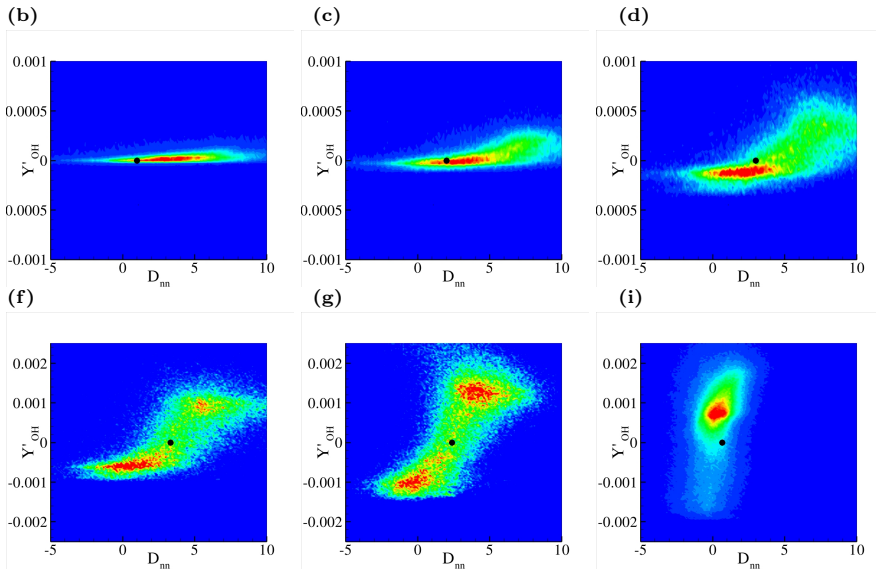


Fig. 8 Joint probability density function (jpdf) in the flame front of the flamelet normalised OH concentration Y'_{OH} (see eq. (7)) and the stress normal to the flame front (deviatoric part) $D_{nn} = E_{dev} : \mathbf{n}\mathbf{n}$. The black circle represents the unstretched laminar flame. Different intervals of H₂ concentration are considered: (b) $8 \times 10^{-3} \leq Y_{\text{H}_2} \leq 1 \times 10^{-2}$; (c) $6 \times 10^{-3} \leq Y_{\text{H}_2} \leq 8 \times 10^{-3}$; (d) $4 \times 10^{-3} \leq Y_{\text{H}_2} \leq 6 \times 10^{-3}$; (f) $2 \times 10^{-3} \leq Y_{\text{H}_2} \leq 3 \times 10^{-3}$; (g) $1 \times 10^{-3} \leq Y_{\text{H}_2} \leq 2 \times 10^{-3}$; (i) $1 \times 10^{-4} \leq Y_{\text{H}_2} \leq 5 \times 10^{-4}$.

modal behavior is retrieved together with a positive correlation between Y'_{OH} and $D_{nn} = 2/3 \partial u_n / \partial n - 1/3 \nabla_\pi \cdot \mathbf{u}_\pi$, where ∇_π is the gradient component tangent to the ideal flame surface. The corresponding unstretched laminar flame, characterized by $D_{nn}^L = 2/3 \partial u_n / \partial n$, is indicated for comparison by the black circles in the figure panels. The most probable states of the turbulent flame are either more active $Y'_{\text{OH}} > 0$ or less active $Y'_{\text{OH}} < 0$ than the laminar flame ($D_{nn} > D_{nn}^L$).

A second relevant aspect is the effect of the local flame curvature,

$$k = \nabla \cdot \mathbf{n} = - \left(\frac{1}{\mathcal{R}_1} + \frac{1}{\mathcal{R}_2} \right) \quad (9)$$

where \mathcal{R}_1 and \mathcal{R}_2 are the principal curvature radii of the flame surface. The curvature helps defining the bulges (negative curvature) and gullies (positive curvature). Figure 9 shows the flame-conditioned jpdf of Y'_{OH} and mean curvature k . Near the fresh gases, panel (b), the curvature has negligible effects on the OH radical concentration. Moving towards the burnt gas region, (c), (d), (f), (g), and (i) panels, the jpdf exhibits an evident negative correlation, confirming that strong burning states occur statistically in regions with prominent negative curvature (bulges), whereas quenching is typical of region with positive curvature (gullies).

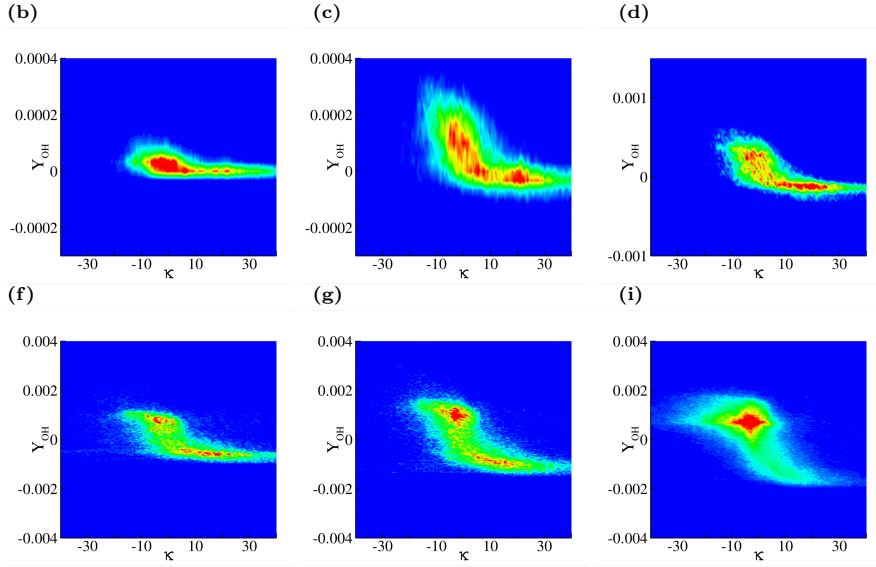


Fig. 9 Joint probability density function (jpdf) of the flamelet normalized OH concentration Y_{OH}' and the local instantaneous curvature of the flame front evaluated by means as the $\nabla \cdot \mathbf{n}$ where \mathbf{n} is the flame front normal $\mathbf{n} = \nabla C_T / |\nabla C_T|$ with C_T the temperature-based progress variable. In order to avoid spurious sampling effects, jpdf are evaluated along the flame front conditioning at different H_2 concentration intervals: (b) $8 \times 10^{-3} \leq Y_{H_2} \leq 1 \times 10^{-2}$; (c) $6 \times 10^{-3} \leq Y_{H_2} \leq 8 \times 10^{-3}$; (d) $4 \times 10^{-3} \leq Y_{H_2} \leq 6 \times 10^{-3}$; (f) $2 \times 10^{-3} \leq Y_{H_2} \leq 3 \times 10^{-3}$; (g) $1 \times 10^{-3} \leq Y_{H_2} \leq 2 \times 10^{-3}$; (i) $1 \times 10^{-4} \leq Y_{H_2} \leq 5 \times 10^{-4}$.

As a further effect the flame curvature may also alter the local ratio between hydrogen and oxygen due to the different diffusion coefficients of the species. This is a well known in laminar lean hydrogen flames where thermo-diffusive instabilities occur. To measure the local equivalence ratio, it is instrumental to define the atomic equivalence ratio, see also [43]. In lean flames the local molecular equivalence ratio decreases up to vanish during the progress of combustion. To quantify the effect of the differential diffusion of the species, an equivalence ratio based on the local number of H and O atoms is defined:

$$\phi = \frac{1}{2} \frac{X_H + X_{OH} + 2 X_{H_2O} + 2 X_{H_2}}{X_O + X_{OH} + X_{NO} + X_{H_2O} + 2 X_{O_2}}, \quad (10)$$

where X_i denotes the molar fraction of the i -specie. This atomic equivalence ratio ϕ is constant during the whole reaction if the species have the same diffusion coefficients. In the present case, a dilution of the unburned mixture may in principle due to entrainment of cold air from the environment. This event however is quite rare since mixing usually takes place only between the hot burnt gases and the cold ambient air. Figure 10 shows the jpdf of ϕ and the mean curvature k inside the flame front for the same Y_{H_2} ranges of figure 7. At the beginning of the flame front, i.e. high Y_{H_2} (panels (b) and (c)), the curvature has negligible effects on the atomic equivalence ratio as shown by

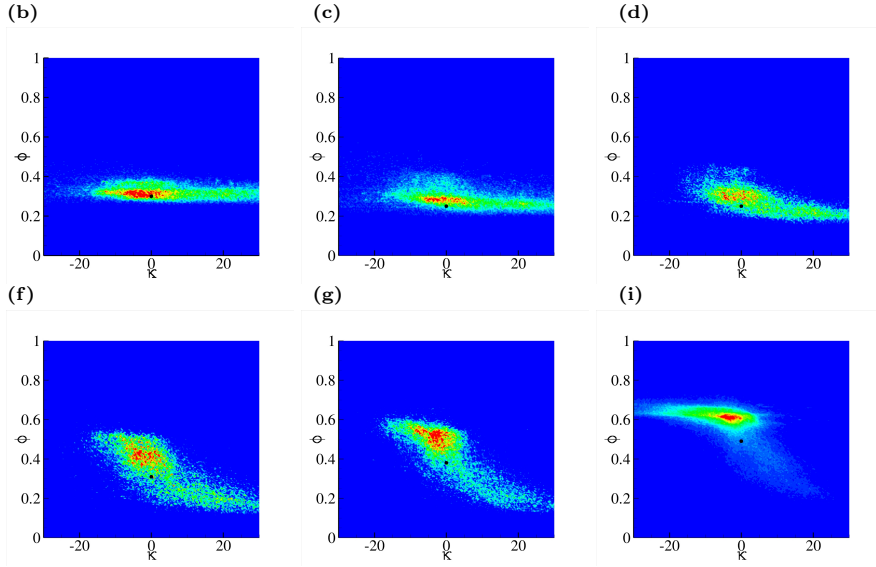


Fig. 10 Joint probability density function (jpdf) of the atomic equivalence ratio between H and O atoms: ϕ , see eq. (10) and the local instantaneous curvature of the flame front evaluated by means as the $\nabla \cdot \mathbf{n}$ where \mathbf{n} is the flame front normal $\mathbf{n} = \nabla C_T / |\nabla C_T|$ with C_T the temperature-based progress variable. The black circle represents the unstretched laminar flame value. In order to avoid spurious sampling effects, jpdf are evaluated along the flame front conditioning at different H₂ concentration intervals: (b) $8 \times 10^{-3} \leq Y_{H_2} \leq 1 \times 10^{-2}$; (c) $6 \times 10^{-3} \leq Y_{H_2} \leq 8 \times 10^{-3}$; (d) $4 \times 10^{-3} \leq Y_{H_2} \leq 6 \times 10^{-3}$; (f) $2 \times 10^{-3} \leq Y_{H_2} \leq 3 \times 10^{-3}$; (g) $1 \times 10^{-3} \leq Y_{H_2} \leq 2 \times 10^{-3}$; (i) $1 \times 10^{-4} \leq Y_{H_2} \leq 5 \times 10^{-4}$.

the jpdf almost flat around the corresponding laminar unstretched value. It should be remarked that in laminar hydrogen flames the atomic equivalence ratio is constant in the burnt and fresh gas regions. However inside the flame front it diminishes, given the preferential diffusion of H₂ which leads to a decrease of hydrogen molar fraction, X_{H_2} , and a slight increase of the oxygen molar fraction, X_{O_2} , (not shown) see e.g. pag. 287 [14] where the phenomenon is accurately described. The corresponding laminar values in each conditioned jpdf is shown by a black circle. In the middle of the flame front, i.e. panels (d)-(f)-(g), the jpdfs show a strong anti-correlation between the curvature and the atomic equivalence ratio. Fronts with positive curvature (gullies) present low values of the atomic equivalence ratio, which is much smaller than the nominal value $\phi = 0.5$ and the corresponding laminar one, leading to the quenched states already highlighted in figure 9. On the contrary, fronts with negative curvature (bulges) exhibit enriched mixtures, that are responsible of the higher chemical activity and the super-adiabaticity as depicted in figure 3. Moreover, we note that the most probable atomic equivalence fraction is usually higher than the corresponding laminar one (black circles) approaching the nominal value of $\phi = 0.5$. In other words, it appears that the turbulent fluctuations contribute to homogenize the mixture towards the nominal equivalence ratio,

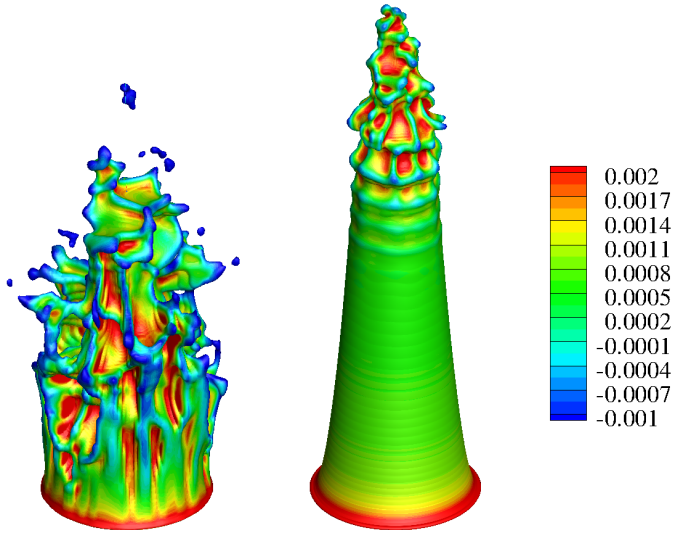


Fig. 11 Instantaneous isosurfaces of turbulent (left) and laminar (right) inflow Bunsen flame. The isosurface corresponds to the $Y_{\text{H}_2} = 0.015$ isosurface and color map refers to the value of the Y'_{OH} , see eq. (7), in the range $0.01 < Y_{\text{H}_2} < 0.02$, corresponding to the case (g) of figure 6, which main feature is the bi-modal distribution of the Y'_{OH} pdf.

i.e. ϕ is often closer to the nominal bulk value than to the laminar unstrained flame value. Approaching the end of the reaction region, panel (i), we note that the most frequent state is that of the bulges with high atomic equivalence ratio. We remark that the departure of the atomic equivalence ratio from its nominal bulk value (the inlet one) occurs only within the flame while the nominal value is recovered ahead and behind the flame.

3.3 Turbulent vs Laminar Bunsen flame comparison

In this subsection we provide a comparison between H_2/Air Bunsen flames fed by a steady laminar and the unsteady turbulent inflow in order to clarify to which extent turbulence affects thermo-diffusive instability. The absence of noise in the laminar inflow prevents to observe transition to turbulence in the present case.

In Figure 11 instantaneous flame surfaces of the turbulent (left) and of the laminar (right) inflow Bunsen flames are reported. The surfaces are $Y_{\text{H}_2} = 0.015$ isosurfaces and are colored by OH radical flamelet fluctuation Y'_{OH} . As expected, under turbulent inflow the flame is shorter indicating that, for a given flow rate, turbulent fluctuations enhance the overall burning speed. The turbulent flame surface is significantly wrinkled while the laminar one presents corrugations only at tip and is smooth in the lower part.

Both flames show super-burning regions. In the turbulent inflow case, flame quenching cusps are present in the gullies, as denoted by the intense negative

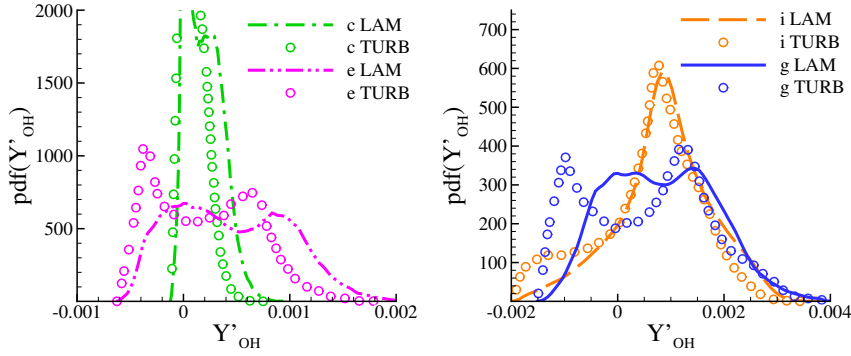


Fig. 12 Probability density function of the OH radical mass flamelet fluctuation, see eq. (6), at 4 of the 8 different H₂ concentration intervals: (c) $6 \times 10^{-3} \leq Y_{\text{H}_2} \leq 8 \times 10^{-3}$; (e) $3 \times 10^{-3} \leq Y_{\text{H}_2} \leq 4 \times 10^{-3}$; (g) $1 \times 10^{-3} \leq Y_{\text{H}_2} \leq 2 \times 10^{-3}$; (i) $1 \times 10^{-4} \leq Y_{\text{H}_2} \leq 5 \times 10^{-4}$. Comparison between the laminar (lines) and the turbulent (symbols) Bunsen flame. For the sake of clarity colors and line styles are kept the same of fig. 6. For the laminar inflow case, only the upper part of the flame, $5 < z/R < 7.5$, (where thermo-diffusive instability is developed) has been considered for statistics.

values of $Y'_{\text{OH}} < 0$, while in the laminar Bunsen flame cusps are almost absent, being $Y'_{\text{OH}} \simeq 0$, i.e. the OH concentration is similar to the planar laminar case.

Figure 11 also illustrates the different paths followed by thermo-diffusive instabilities in laminar and turbulent flames. In laminar Bunsen flames, the instability slowly evolves moving downstream. First perturbations originate and grow in planes normal to the jet axis, then typical cellular-like structures form and eventually mutually interact losing their regularity near the flame tip. The turbulent case is strongly influenced by the turbulent coherent structures issued by the turbulent pipe flow. In particular, the quasi-streamwise vortices together with the low- and high- speed streaks living near the pipe wall are much stronger than the small scale turbulence in the jet core and (see e.g. [44,45]) control the front curvature in the lower part of the flame, triggering corrugations parallel to the flow direction. These corrugations generate super-burning and quenched regions via the thermo-diffusive instabilities. Further downstream the front becomes more and more corrugated as expected of a fully turbulent flow.

The statistical characterization of these behaviors is discussed. For the two cases figure 12 provides the probability density function of Y'_{OH} conditioned to different H₂ concentration levels. In interval (c), i.e. near the fresh gas, fig. 12 left panel, a mono-modal behavior similar to the turbulent case is noted for the laminar Bunsen flame, though with more frequent positive strong events than the turbulent case. In other words, the laminar flame shows relatively more regions with intense reaction rate and higher flamelet fluctuation of OH concentration than the turbulent one. Different is the behavior well inside the flame front, e.g. in the intervals (e) and (g), where the turbulent

inlet case shows the discussed bi-modal distribution which is either absent or strongly reduced in the laminar case. In particular, in interval (e), left panel of fig. 12, the negative fluctuation peak of the turbulent case does not appear for the laminar flame. The pdf of Y'_{OH} for the laminar Bunsen flame is almost flat between zero and small positive values showing relatively more frequent strong super-burning regions. The conditioning interval (g), $1. \times 10^{-3} \leq Y'_{\text{H}_2} \leq 2. \times 10^{-3}$, correspond to the isosurfaces shown in fig. 11 ($Y'_{\text{H}_2} \leq 1.5 \times 10^{-3}$). As observed, negative values of Y'_{OH} are less frequent than the turbulent case with an even flatter pdf. A similar trend is found towards the end of the reaction front, interval (i), where the probability to find negative OH flamelet fluctuations is smaller than the turbulent case.

In conclusion, though the thermo-diffusive instability crucially affects both turbulent and laminar flames, the presence of turbulent structures deeply alter its dynamics. The laminar OH concentration pdf is always mono-modal with no negative peak, implying that quenched regions are statistically irrelevant. Indeed turbulence is the source of the observed bimodal behavior, fig. 6. The turbulent fluctuations produce corrugations of the flame front that in turn trigger the thermo-diffusive instability. The probability of negative OH concentration flamelet fluctuations becomes significant, implying local quenching associated with positive curvature (gullies). Apparently, while super-burning regions are naturally developed by the thermo-diffusive instability even in laminar flames, only the turbulence triggers local flame quenching. We have observed that the thermo-diffusive instability slowly grows from its inception at base up to flame tip where disturbances become three-dimensional. Turbulent fluctuations are instead much faster and sufficiently strong to prevent the formation of the thermo-diffusive cellular structures thereby setting the time scale of the turbulent flame.

4 Final remarks

The paper discusses DNS data of a turbulent Bunsen flame of a lean premixed mixture of molecular hydrogen and air. The turbulent combustion appears to be mainly characterized by two states: strong burning cells alternating with nearly quenched regions. Both the instantaneous behavior and the statistical investigation suggest that the strong burning cells are associated with the bulges, namely the regions convex towards the fresh gases (negative curvatures), while almost all quenched areas are associated with the gullies, regions convex towards the burnt gases (positive curvatures). To better characterize this behavior we have used a statistical analysis conditioned to the local hydrogen concentration in order to move through the local reaction region from fresh to burnt gases. Well inside the flame front, the statistical occurrence of the bi-modal states exceeds the incidence of the corresponding laminar planar one, so that the flame may be considered mainly constituted by these two states. A positive correlation is detected between the deviatoric strain rate and the local chemical activity; moreover, the expansion induced by the heat release produces a larger deformation in the direction normal to the flame

front, localized in the strong burning cells. The analysis of the front curvature suggests that the origin of such bi-stable behavior is related to the thermo-diffusive instabilities. The local curvature of the front, combined with the different transport properties of the species, induces a local enrichment/dilution of the mixture and it results in strong burning cells (bulges) and quenched regions (gullies). The local curvature was shown to correlate with the local equivalence ratio and produces the observed bimodal behavior. In addition, the enrichment/depletion of the local mixture is spatially alternated along the flame front. Since the bulk equivalence ratio of the mixture was fixed to be $\Phi = 0.5$, the local enrichment and depletion of the mixture correspond to an increase/decrease of the adiabatic combustion temperature. The picture emerging from the present moderate Reynolds number simulation is consistent with the turbulent fluctuations initially corrugating the flame front and triggering the instabilities which successively affect the local chemical activity.

Besides the regions well inside reaction zone, in the flame region closest to the fresh and burn gases, a mono-modal behavior similar to the unstretched laminar flame is detected. However, the bi-stable dynamics influences the process also in these external parts of the flame as indicated by the strong pdf tails of the flamelet OH concentration.

A comparison between the turbulent and a laminar inflow Bunsen flame was able to better assess the effect of turbulent fluctuations. The laminar flame shows a clear cellular shape near the tip, purely induced by the thermo-diffusive instability. Differently from the turbulent flame, the laminar flame process is always mono-modal. Actually we found a high statistical incidence of the super-burning state, but not locally quenched regions. We infer that the super-burning behavior naturally develops via thermo-diffusive instability even without turbulent fluctuations, which are instead necessary to originate quenched regions triggering the formation of gullies.

These results are expected to be relevant in the context of modeling turbulent flames at low Lewis numbers by means of the flamelet assumption, since the local flame features are frequently and markedly different from the unstretched laminar flame. In particular, flame models should comply with the bi-stable nature of the turbulent flame which is mainly characterized by two alternative local states, the super-adiabatic and the almost quenched state.

References

1. M. Chaos, F. Dryer, *Combustion Science and Technology* **180**(6), 1053 (2008)
2. A. Aspden, M. Day, J. Bell, *Journal of Fluid Mechanics* **680**, 287 (2011)
3. N. Chakraborty, R. Cant, *Physics of Fluids* **21**, 035110 (2009)
4. O. Gicque, D. Thévenin, N. Darabiha, *Flow, turbulence and combustion* **73**(3-4), 307 (2005)
5. A. Vreman, J. Van Oijen, L. De Goey, R. Bastiaans, *International Journal of Hydrogen Energy* **34**(6), 2778 (2009)
6. H. Wang, K. Luo, J. Fan, *Energy & Fuels* **27**(1), 549 (2012)
7. H. Wang, K. Luo, K. Qiu, S. Lu, J. Fan, *International Journal of Hydrogen Energy* **37**(6), 5246 (2012)

8. S. Chung, C. Law, *Combustion and Flame* **52**, 59 (1983)
9. C. Law, S. Chung, *Combustion Science and Technology* **29**(3-6), 129 (1982)
10. A. Lipatnikov, J. Chomiak, *Combustion science and technology* **137**(1-6), 277 (1998)
11. A. Lipatnikov, J. Chomiak, *Progress in Energy and Combustion Science* **31**(1), 1 (2005)
12. J. Yuan, Y. Ju, C. Law, *Physics of Fluids* **17**, 074106 (2005)
13. T. Poinsot, D. Veynante, *Theoretical and numerical combustion* (RT Edwards, Inc., 2005)
14. C. Law, *Combustion physics* (Cambridge University Press, 2006)
15. N. Chakraborty, E. Hawkes, J. Chen, R. Cant, *Combustion and Flame* **154**(1), 259 (2008)
16. T. Mantel, R. Borghi, *Combustion and Flame* **96**(4), 443 (1994)
17. Y. Shim, S. Tanaka, M. Tanahashi, T. Miyauchi, *Proceedings of the Combustion Institute* **33**(1), 1455 (2011)
18. H.G. Im, J.H. Chen, *Combustion and flame* **131**(3), 246 (2002)
19. R. Bastiaans, A. Vreman, *International Journal of Numerical Methods for Heat & Fluid Flow* **22**(1), 112 (2012)
20. M. Day, J. Bell, P.T. Bremer, V. Pascucci, V. Beckner, M. Lijewski, *Combustion and Flame* **156**(5), 1035 (2009)
21. A. Majda, J. Sethian, *Combustion science and technology* **42**(3-4), 185 (1985)
22. F. Battista, F. Picano, C.M. Casciola, *Physics of Fluids (1994-present)* **26**(5), 055101 (2014)
23. N. Waterson, H. Deconinck, *Journal of Computational Physics* **224**(1), 182 (2007)
24. I. Orlanski, *Journal of computational physics* **21**(3), 251 (1976)
25. F. Picano, C. Casciola, *Physics of Fluids* **19**(11), 118106 (2007)
26. B. Boersma, G. Brethouwer, F. Nieuwstadt, *Physics of fluids* **10**, 899 (1998)
27. X. Li, J. Demmel, J. Gilbert, iL. Grigori, M. Shao, I. Yamazaki, *SuperLU Users' Guide*. Tech. Rep. LBNL-44289, Lawrence Berkeley National Laboratory (1999). <http://crd.lbl.gov/~xiaoye/SuperLU/>. Last update: August 2011
28. F. Picano, K. Hanjalić, *Flow, turbulence and combustion* **89**(4), 627 (2012)
29. F. Picano, G. Sardina, P. Gualtieri, C. Casciola, *Physics of Fluids* **22**, 051705 (2010)
30. F. Battista, F. Picano, G. Troiani, C. Casciola, *Physics of Fluids* **23**(12), 123304 (2011)
31. F. Picano, F. Battista, G. Troiani, C. Casciola, *Experiments in Fluids* **50**(1), 75 (2011)
32. C. Bowman, R.K. Hanson, D.F. Davidson, W. Gardiner Jr., V. Lissianski, G.P. Smith, D. Golden, M. Frenklach, M. Goldenberg. *Gri-mech home page* (1999). URL <http://www.me.berkeley.edu/gri-mech/>
33. J. Chen, W. Chang, M. Koszykowski, *Combustion science and technology* **110**(1), 505 (1995)
34. J. Hirschfelder, C. Curtiss, R. Bird, *Molecular Theory of Gases and Liquids* (John Wiley and Sons, Inc., New York, 1964)
35. Y.C. Chen, R.W. Bilger, *Combustion and flame* **131**(4), 400 (2002)
36. Y.C. Chen, R.W. Bilger, *Combustion and flame* **138**(1), 155 (2004)
37. J.H. Frank, P.A. Kalt, R.W. Bilger, *Combustion and Flame* **116**(1), 220 (1999)
38. S. Stårner, R. Bilger, K. Lyons, J. Frank, M. Long, *Combustion and flame* **99**(2), 347 (1994)
39. N. Chakraborty, M. Klein, N. Swaminathan, *Proceedings of the Combustion Institute* **32**(1), 1409 (2009)
40. C. Altantzis, C. Frouzakis, A. Tomboulides, S. Kerkemeier, K. Boulouchos, *Proceedings of the Combustion Institute* **33**(1), 1261 (2011)
41. S. Kadowaki, T. Hasegawa, *Progress in energy and combustion science* **31**(3), 193 (2005)
42. G. Barenblatt, Y.B. Zeldovich, A.G. Istratov, *Zh. Prikl. Mekh. Tekh. Fiz* **4**, 21 (1962)
43. J.B. Bell, R.K. Cheng, M.S. Day, I.G. Shepherd, *Proceedings of the Combustion Institute* **31**(1), 1309 (2007)
44. S.K. Robinson, *Annual Review of Fluid Mechanics* **23**(1), 601 (1991)
45. L. Brandt, *European Journal of Mechanics-B/Fluids* (2014)